

© by Randy J. Chase

EVALUATION OF TRIPLE-FREQUENCY RADAR RETRIEVAL OF SNOWFALL
PROPERTIES USING COINCIDENT AIRBORNE IN-SITU OBSERVATIONS DURING
OLYMPEX

BY

RANDY J. CHASE

THESIS

Submitted in partial fulfillment of the requirements
for the degree of Master of Science in Atmospheric Sciences
in the Graduate College of the
University of Illinois at Urbana-Champaign, 2018

Urbana, Illinois

Advisers:

Associate Professor Stephen W. Nesbitt
Professor Greg M. McFarquhar

ABSTRACT

Particle scattering models have shown that aggregates and spherical particles occupy distinct regions of the Ku-Ka-W-band Dual-Frequency Ratio (DFR) plane. Furthermore, ground-based observations suggest that particle bulk density and characteristic size can be retrieved from the DFR plane. This is the first study to evaluate the retrieval of particle shape, bulk density and characteristic size using airborne triple-frequency radar observations coincident with airborne in-situ microphysical measurements. Data from the Olympic Mountains Experiment (OLYMPEX) resulted in 2.2 hours of observations that showed the Ku-Ka-W DFR plane offered little unambiguous information about particle shape. Analysis of a case study on 3 December 2015 is consistent with a past modeling study, showing increased bulk density with increased DFR between the Ka- and W-band. Meanwhile, bulk statistics are consistent with a past observational study, showing the potential retrieval of effective density and characteristic size from the DFR Ku-Ka-W plane.

ACKNOWLEDGEMENTS

Funding for this research was provided by NASA Precipitation Measurement Missions grant NNX16AD80G under Ramesh Kakar. A portion of the research described in this paper was carried out at the Jet Propulsion Laboratory, California Institute of Technology, under contract with the National Aeronautics and Space Administration. We thank all the participants of OLYMPEX for collecting the data used in this study. All data used in this investigation are found on the NASA GHRC OLYMPEX data archive doi:

<http://dx.doi.org/10.5067/GPMGV/OLYMPEX/DATA101>. The matching software to match the

Citation and the radar gates can be found here doi: <https://zenodo.org/badge/latestdoi/113089990>

PLAIN LANGUAGE SUMMARY

Currently, remote sensing retrievals of ice-clouds require assumptions since particle shape and size vary greatly in the atmosphere. Additionally, particle shape and size constrain relationships of mass and fall velocity of ice within a cloud, which affect remote sensing retrievals. Modeling studies have shown that the scattering characteristics of complex ice particles, (e.g., aggregates) have a distinct scattering signature when compared to the same size particles represented as spheres using three frequencies. Thus, there is potential to retrieve information about particle shape using triple-frequency radar observations to constrain the assumptions of particle shape in the ice cloud retrieval.

This thesis is the first study to use airborne triple-frequency radar observations coincident with airborne in-situ microphysical measurements to evaluate both the scattering signal discussed and retrievals of characteristic size and effective density. We found that most of the observations from the Olympic Mountains Experiment (OLYMPEX) do not show the unique scattering signal of aggregates, limiting the value of triple-frequency observations to improve assumptions about particle shape. Furthermore, while the triple-frequency observations confirm relationships with particle size and effective density outlined in a previous study, most of the variation in characteristic size and bulk effective density is captured by two frequencies.

NOTA BENE

This thesis was submitted to the American Geophysical Union's Geophysical Research Letters on 19, March 2018. The citation is as follows:

Chase, R. J., Finlon, J. A., Borque, P., McFarquhar, G. M., Nesbitt, S. W., Tanelli, S., Sy, O. O., Durden, S. L. and Poellot, M. 2018: Evaluation of triple-frequency radar retrieval of snowfall properties using coincident airborne in-situ observations during OLYMPEX. *Geophys. Res. Lett.* *In review.*

TABLE OF CONTENTS

CHAPTER 1: INTRODUCTION	1
CHAPTER 2: METHODOLOGY	4
2.1 Radar	4
2.2 Microphysics	4
2.3 Co-locating radar and in-situ observations	6
2.4 Calibration and Attenuation Correction	7
2.5 Matched Particle Size Distribution Representativeness	8
2.6 Figures	10
CHAPTER 3: RESULTS & DISCUSSION	16
3.1 Case Study: 3 December 2015	16
3.2 DFR plane and bulk statistics	17
3.3 Figures	19
CHAPTER 4: CONCLUSIONS	21
REFERENCES	23

CHAPTER 1: INTRODUCTION

The development of active and passive satellite precipitation remote sensing has allowed for characterization of weather systems around the world, including over the ocean and less populated areas where ground-based measurements are sparse. Spaceborne radar enables the retrieval of cloud and precipitation structure which is valuable for evaluating numerical model simulations (e.g., Delanoë et al., 2011; Stein et al., 2015). Furthermore, the retrieval of precipitation rate of ice (R) and ice water content (IWC) can characterize the global distribution of ice-phase precipitation, which is needed to understand the global water and energy budget. The retrieval of R and IWC requires assumptions about particle shape, size, mass, and particle terminal fall velocity. The use of multiple radar frequencies, one predominately in the Rayleigh scattering regime and at least one in the Mie regime, has been investigated to constrain assumptions made in R and IWC retrievals. Kneifel et al. (2011) found that scattering models of complex particles such as aggregates and dendrites occupy distinct regions of the triple-frequency Dual-Frequency Ratio (DFR) Ku-Ka (DFR_{Ku-Ka}) and Ka-W (DFR_{Ka-W}) two-dimensional phase space when compared to models of soft spheres and spheroids. Models of aggregates and dendrites (e.g., Petty & Huang, 2010; Leinonen & Szyrmer, 2015) have shown that as the particle maximum dimension (D) increases, there is an increase then a decrease of DFR_{Ka-W} while DFR_{Ku-Ka} increases continually. This creates a *hook* signature in the triple-frequency DFR plane. Dissimilarly, using soft spheres and spheroid models (e.g., Austin et al., 2009; Matrosov, 2007) results in a continual increase of both DFR_{Ka-W} and DFR_{Ku-Ka} with increasing D and therefore, no *hook* signature. Thus, the triple-frequency DFR plane can be

potentially used to determine regions dominated by complex particles (e.g. aggregates or dendrites).

Moreover, a portion of the triple-frequency observations collected over Wakasa Bay, Japan could be explained by the *hook* produced from aggregate and dendrite scattering models (Kulie et al., 2014; Leinonen et al., 2012). Despite the importance of these results, direct in-situ evaluation of the inferences from scattering models of aggregates has remained largely elusive. One exception however, is the recent study by Kneifel et al. (2015), which used a surface disdrometer and triple-frequency range gates within 200 m of the surface to compare snowfall characteristics with triple-frequency signatures in southern Finland. When aggregates were observed at the surface, DFR values followed the *hook* of the aggregate and dendrite models, whereas when spherical particles were seen the DFR values followed those respective models. Despite this first claim of consistency between scattering models and observed DFR, more testing of the triple-frequency phase space is needed for different particle habits, which depend on variable meteorological conditions where varying microphysical processes may dominate.

Additional bulk microphysical quantities such as effective bulk density (ρ_e) and characteristic particle size have been suggested as viable retrievals from the DFR plane. Analysis of ground based in-situ observations have shown that higher ρ_e results in increased DFR_{Ka-W} and decreased DFR_{Ku-Ka} , effectively rotating the DFR curve (Kneifel et al., 2015). Furthermore, a recent modeling study (Leinonen & Szyrmer, 2015) varying the degree of riming on aggregates showed quasi-consistent results with Kneifel et al.'s (2015) study regarding larger amounts of rime ice, and thus larger ρ_e , leading to higher DFR_{Ka-W} and little to no change in DFR_{Ku-Ka} . While these studies provide some evidence to support bulk microphysical retrievals, additional observations aloft and in different regimes are still necessary for a more thorough evaluation.

The Olympic Mountains Experiment (OLYMPEX), conducted in late 2015 over the west coast of Washington State and the nearby coastal region (Houze et al., 2017), obtained triple-frequency radar observations coincident with in-situ cloud microphysical measurements. In this study, airborne coincident triple-frequency radar and in-situ microphysical observations are used to determine if scattering models produce consistent results on the Ku-Ka-W-band DFR plane for various regions of stratiform clouds, which have ice particles of varying habits and sizes. Observations from OLYMPEX provide 2.2 hours of in-cloud data with Ku-, Ka- and W- band radar observations coincident with in-situ aircraft data characterizing particles and their bulk properties.

CHAPTER 2: METHODOLOGY

2.1 Radar

To provide radar data coincident with in-situ microphysics observations, the National Aeronautics and Space Administration (NASA) DC-8 aircraft carrying the Airborne Precipitation Radar Third Generation (APR-3) flew mostly constant altitude flights above the University of North Dakota (UND) Citation aircraft (Map, Figure 1). The Citation was outfitted with instruments that measured state parameters (e.g., temperature, pressure), bulk cloud properties (e.g., total water content *TWC*) and the particle size distribution (PSD). The APR-3 observations allowed for simultaneous scanning measurements of Ku- (13.4 GHz), Ka- (35.6 GHz) and W- (94.9 GHz) band reflectivity $\pm 25^\circ$ from nadir with 30 m vertical sampling. Measured reflectivity values were corrected for attenuation and adjusted for calibration using the method described in Section 2.4.

2.2 Microphysics

The PSD was measured onboard the Citation using a combination of two optical array probes: the vertically-oriented portion of a 2-Dimensional Stereo (2DS) probe and a vertically-oriented High Volume Precipitation Spectrometer Version 3 (HVPS3). To minimize the influence of shattered artifacts in the PSDs, both the 2DS and HVPS3 had anti-shattering tips and the data were processed with the University of Illinois/Oklahoma Optical Array Probe Processing Software (UIOOPS), using particle inter-arrival times to identify shattered artifacts from the 2DS data (Field et al., 2003; Jackson et al., 2014). Here, the 2DS is used to determine the number distribution function, $N(D)$, for particles with D between 225 μm and 1 mm while the HVPS3 is used for D between 1 mm and 3.25 cm. The lower bound for the $N(D)$ using the 2DS is chosen based on the observation of supercooled drizzle drops ($D \cong 200 \mu\text{m}$, Figure 7g)

which ensures the calculations using the PSD are mostly characteristic of ice. Further, the absence of smaller particles should not have a major impact on calculated ice mass or reflectivity which are dominated by larger particles. A 5 s moving average of the PSD is applied 2 s before and after each point when and where the Citation aircraft is regarded as coincident with the radar gate (Section 2.3).

Several bulk microphysical quantities are calculated from the PSD in order to evaluate the retrieval of ρ_e and characteristic size. For this study, ρ_e is the ratio of the mass of ice to the total volume of ice (V) within some sample volume. Since there is no method of directly deriving ρ_e from 2-D images obtained by the 2DS and HVPS3, it is defined as

$$\rho_e = \frac{TWC}{V}, \quad (1)$$

where V is defined as the sum of the volume enclosed by an ellipsoid with an aspect ratio, α , of 0.6 (Hogan et al., 2012) of all particles within the PSD and TWC is the total water content from all particles within the PSD. Mathematically, V can be described as

$$V = \frac{\pi}{6} \int_{D_{min}}^{D_{max}} N(D) \alpha^2 D^3 dD, \quad (2)$$

and TWC as

$$TWC = \int_{D_{min}}^{D_{max}} N(D) a D^b dD. \quad (3)$$

The calculation of TWC from the PSD requires a mass-Dimension (m - D) relation which provides the a and b values in Equation 3. To investigate the sensitivity of the computed TWC to the choice of relation, two relationships are used here and discussed in Section 2.4: Brown and Francis (1995) modified by converting its original particle size definitions to D following Hogan et al. (2012) (hereafter BF95); and Heymsfield et al. (2004) (hereafter HY04).

The characteristic size chosen for this study is the median mass dimension (D_{mm}), which is defined as the dimension where 50% of the accumulated TWC is less than D_{mm} and 50% greater than D_{mm} . This characteristic size is used to evaluate the retrieval of D_{mm} suggested by Kneifel et al. (2015) in Section 3.2.

2.3 Co-locating radar and in-situ observations

Fifteen flight legs with temperatures lower than -0.5 °C within stratiform clouds were sampled representing 2.2 hours of cloud observations when the APR-3 aboard the DC-8 sampled the same region as the Citation. In-situ observations were assumed to be characteristic of the entire matched radar volume despite the differences in sample volume between the radar and the in-situ probes. Here radar volumes collected within 10 minutes temporally and 1 km spatially of the Citation are regarded as collocated. Furthermore, analysis is restricted to periods when the total number concentration (N_t) was greater than 10^3 m^{-3} to ensure that the Citation was within cloud.

To find the instances of collocation, a k -dimensional-tree searching algorithm was used. The Barnes (1964) interpolation technique was then applied to 30 of the closest radar gates within 1 km of the Citation location. Additionally, any radar gate contaminated by the skin paint of the Citation or any other outlier was removed using the following statistical definition of an outlier:

$$\text{Outlier} > \text{Median} + 1.5 * \text{Interquartile range} \quad (4)$$

$$\text{Outlier} < \text{Median} - 1.5 * \text{Interquartile range} \quad (5)$$

Furthermore, if the standard deviation of the 30 gates was greater than 3 dB, the cloud element was regarded as heterogeneous and the point was not used. For additional quality control the bright-band, rain echoes, radar artifacts and the surface return were identified and removed from

the radar data before matching. To test the sensitivity of the number of gates in the average, the difference between using the closest gate and 30 gates was calculated and was on average less than 0.1 dB (Figure 2).

2.4 Calibration and Attenuation Correction

Calibration of the measured reflectivity at the 3 frequencies is required before any analysis of DFR can be conducted. In theory, the same reflectivity should be measured for all 3 frequencies for small ice particles near cloud top where attenuation is low and particles are scattering in the Rayleigh regime. Data between 10 dBZ and 15 dBZ near echo tops were used to compare the Ku-band to the Ka-band and data between -10 dBZ and 0 dBZ were used to compare Ka- to W- band. An example of this method is shown in Figure 3. The second method used clear air observations of the ocean surface backscatter cross-section (Tanelli et al., 2006). The relative uncertainty in calibration is estimated to be 0.5 dB to 1 dB for Ku-Ka and Ka-W respectively.

To compare the observed multi-frequency radar observations with in-situ data on the DFR plane against scattering models, a correction for two-way attenuation at the W-band caused by supercool liquid water (LWC), atmospheric constituents (e.g., O_2) and ice scattering must be performed. Corrections based on path-integrated attenuation are not possible for the flight legs examined because some flights were over complex terrain. Thus, to correct for the absorption due to LWC , in-situ measurements of LWC observed by the King probe for each flight are used to create a median profile of LWC (Figure 4a), which is then used to calculate the specific attenuation using the coefficients from Meneghini and Kozu (1990). It is noted that the King probe could be overestimating LWC because of its interaction with ice (e.g., Cober et al., 2001) and underestimating LWC in the presence of drizzle drops (e.g., Strapp et al., 2003,

Schwarzenboek et al., 2009). No correction is applied to the LWC due to these uncertainties. Path integrated attenuation due to LWC is estimated to be on the order of 1 – 1.5 dB. To correct for absorption from atmospheric water vapor and diatomic oxygen the coefficients from the 2013 manual by the Radiocommunication Sector of International Telecommunication Union and observed radiosonde soundings launched from Quillayute Airport, near the coast of Washington State that were closest in time to the beginning of each flight leg, are used. The correction magnitude for gaseous absorption above the melting level is estimated to be on the order of 1 dB. Correction for extinction from ice scattering at W-band (negligible at the other frequencies) is preformed using the Kulie et al. (2014) relationship derived between extinction and Ku-band reflectivity factor. The correction from ice extinction makes up the remaining total attenuation correction shown in Figure 4b. Median path integrated attenuation correction at W-band is estimated to be on the order of 3.5 – 9 dB. Attenuation correction at the other wavelengths (Ku-, Ka- band) are only preformed for the atmospheric gases and are on the order of 0.1 and 0.5 dB for Ku- and Ka-band respectively.

2.5 Matched Particle Size Distribution Representativeness

In order to assess how well the matched PSD and the subsequent calculations of D_{mm} and ρ_e represent particles within the radar gates, the Ku-band reflectivity is forward modeled from the observed PSD using the Rayleigh-Gans sphere approximation (Hogan et al., 2012) and the m - D relations noted in Section 2.2. The Ku-band is chosen because it experiences the least amount of attenuation and non-Rayleigh scattering effects. Calculated reflectivity using BF95 has a persistent underestimation when compared to the coincident Ku-band radar reflectivity with a mean difference of – 7.8 dB and a correlation of 0.7. The same comparison using the m - D from HY04 provides an improved match with a mean difference of +0.48 dB and a correlation of 0.71

(see Figure 5). Since this study is focused on radar, the HY04 relation is used henceforth to calculate the D_{mm} and ρ_e . A sensitivity test comparing D_{mm} and ρ_e when using the BF95 has a correlation of 0.99 and an average ratio of 1.05 and 2 for D_{mm} and ρ_e respectively compared to HY04 (Figure 6). Thus, the effect of choice of m - D will not affect the overall trends in terms of linear correlation, but can affect the magnitude of those trends.

2.6 Figures

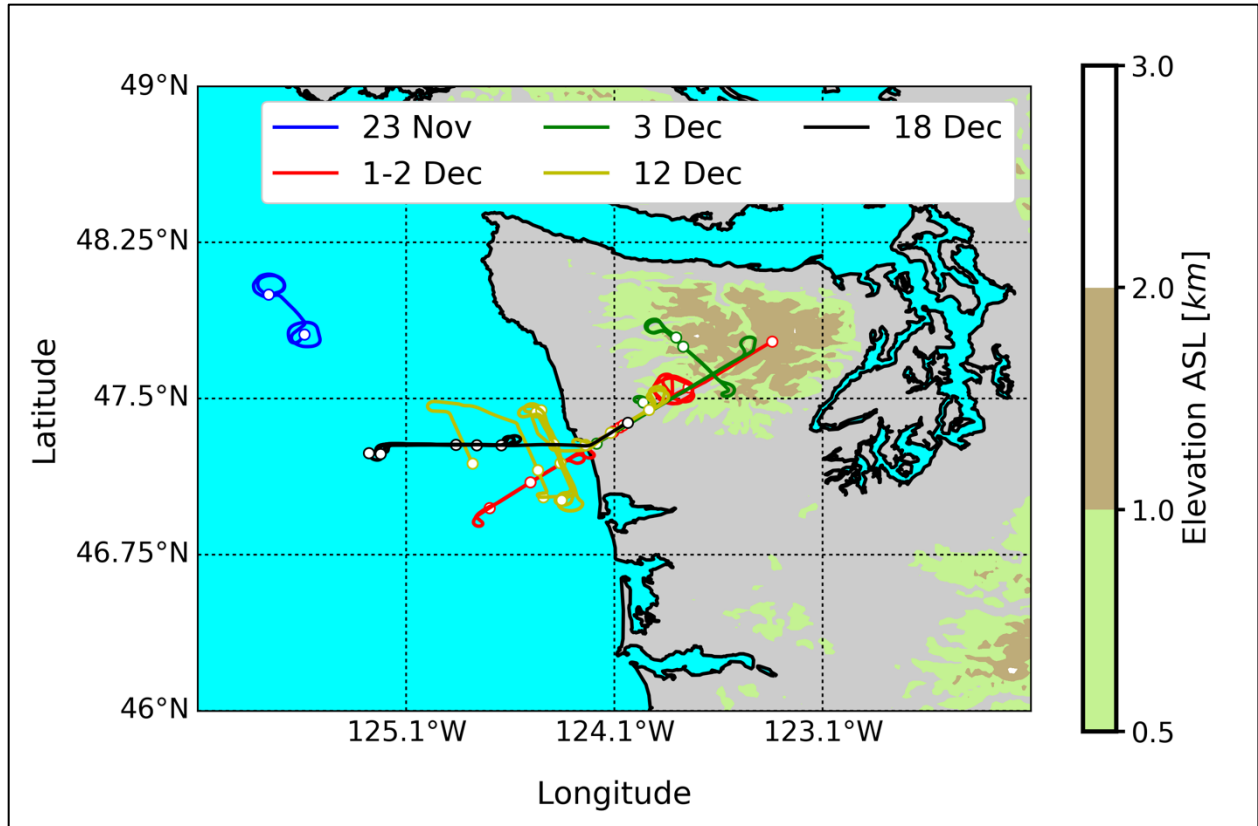


Figure 1. Map of flight tracks of the University of North Dakota Citation where there are coincident radar gates from the APR-3. Each color corresponds to a different day. Contours (not blue or grey) are the elevation above sea level.

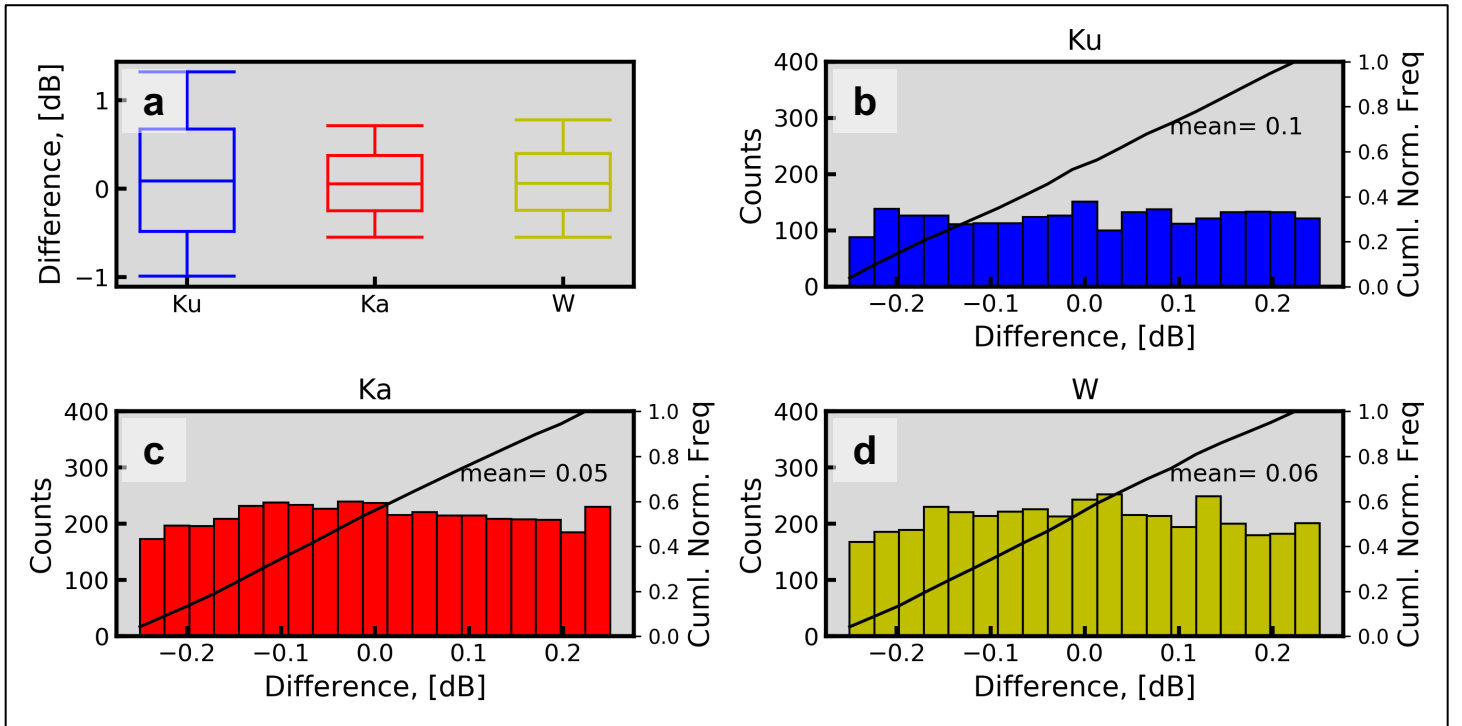


Figure 2. Comparing averaging techniques of the radar data matched to the Citation location. Each subplot contains the subtraction of the closest gate from the 30 gate Barnes average. **(a)** Boxplot is the 10th, 25th, 50th, 75th and 90th percentile. Left on histograms **(b-d)** are the raw counts (bars), right is the cumulative normalized frequency (curve). **(b)** Histogram of Ku-band difference **(c)** Histogram of Ka-band difference **(d)** Histogram of W-band difference.

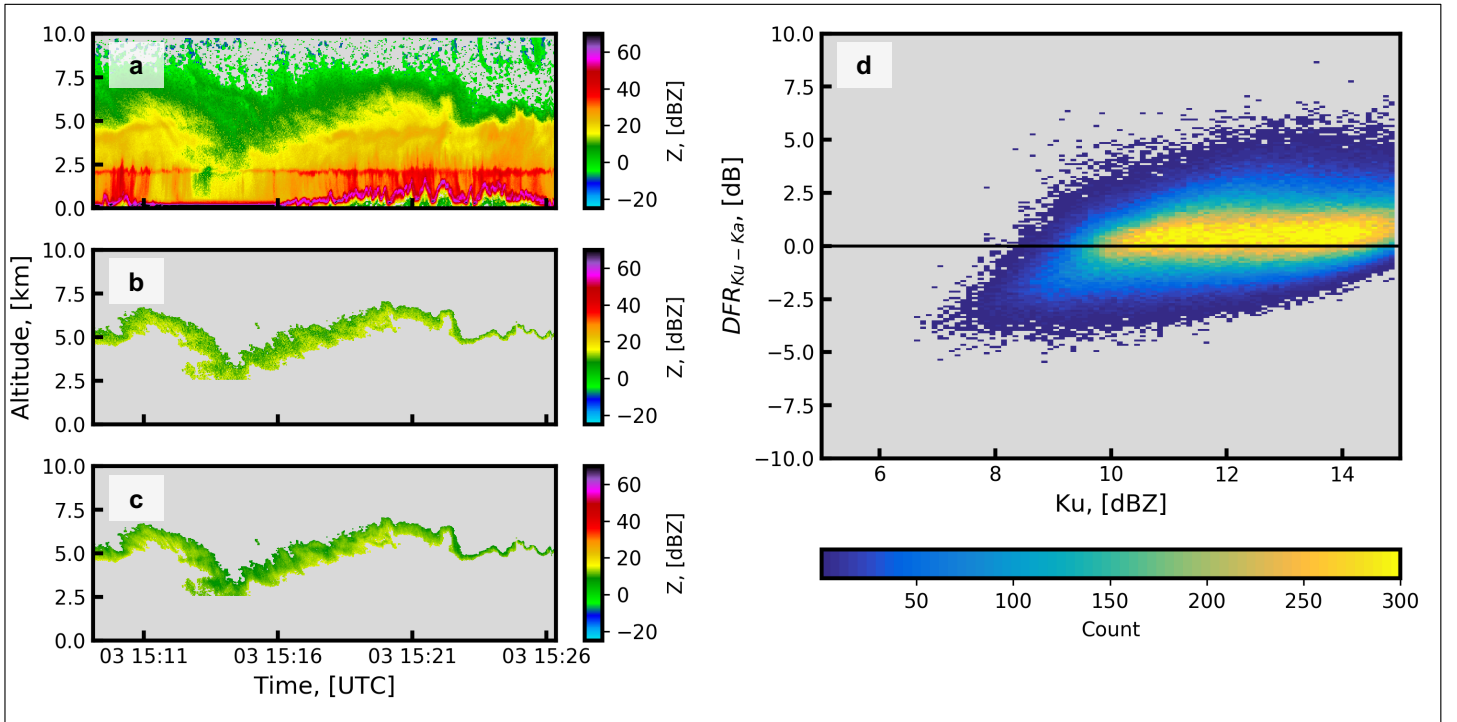


Figure 3. Calibration assessment of two frequencies on the APR-3. (a) Raw Ku-reflectivity measured on 3 December 2015 at 1509. (b) Gaseous attenuation corrected Ku-reflectivity masked to get rid of cloud top noise, and where the Gaussian 1σ smoothed Ku is between 10 dBZ and 15 dBZ. (c) Gaseous attenuation corrected Ka-reflectivity masked to get rid of cloud top noise, and where b is masked. (d) Two-dimensional frequency histogram of the subtraction of c from b, as a function of b.

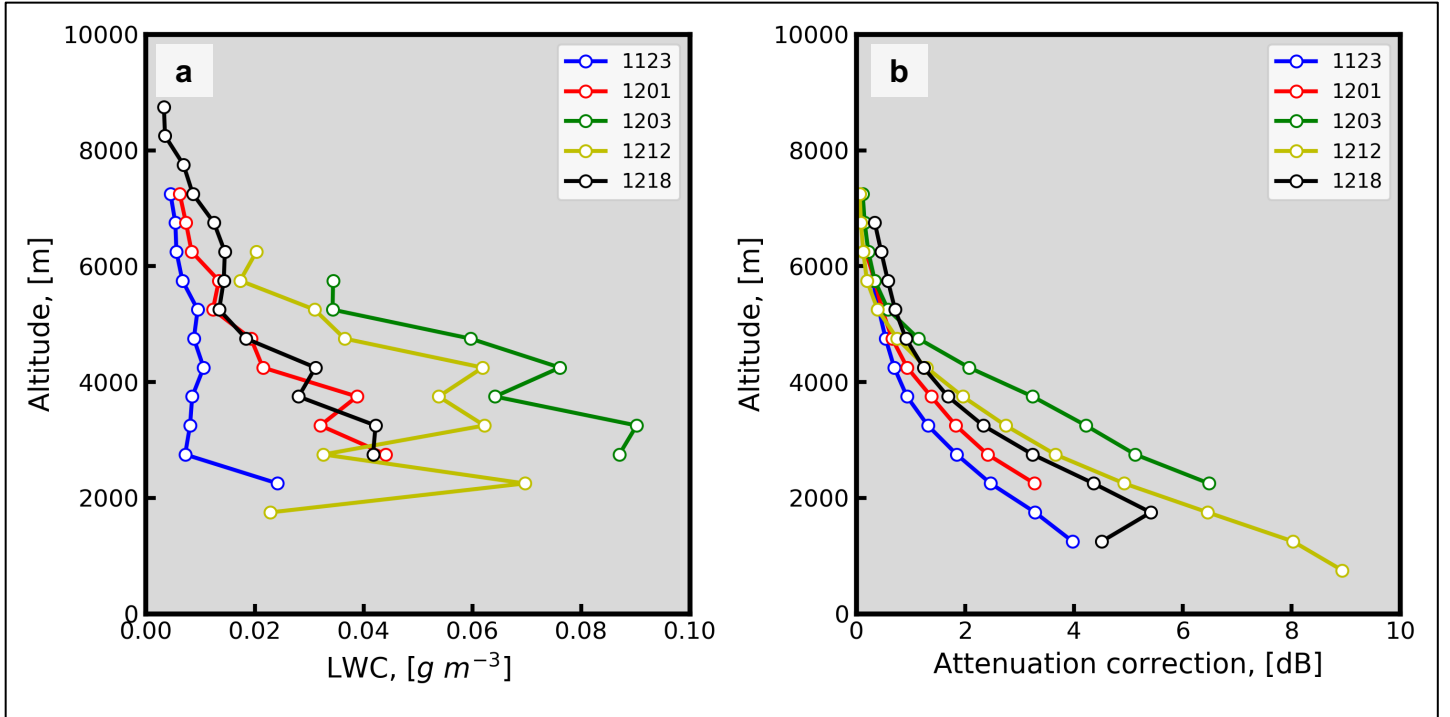


Figure 4. Attenuation correction method. **(a)** Observed LWC measured by King hot wire probe as a function of altitude. Each line represents the median LWC for 500 m bins with temperatures less than $-5\ ^\circ\text{C}$. The colors correspond to the dates indicated in the legend. **(b)** The cumulative median correction for W-band reflectivity as a function of altitude on each flight day.

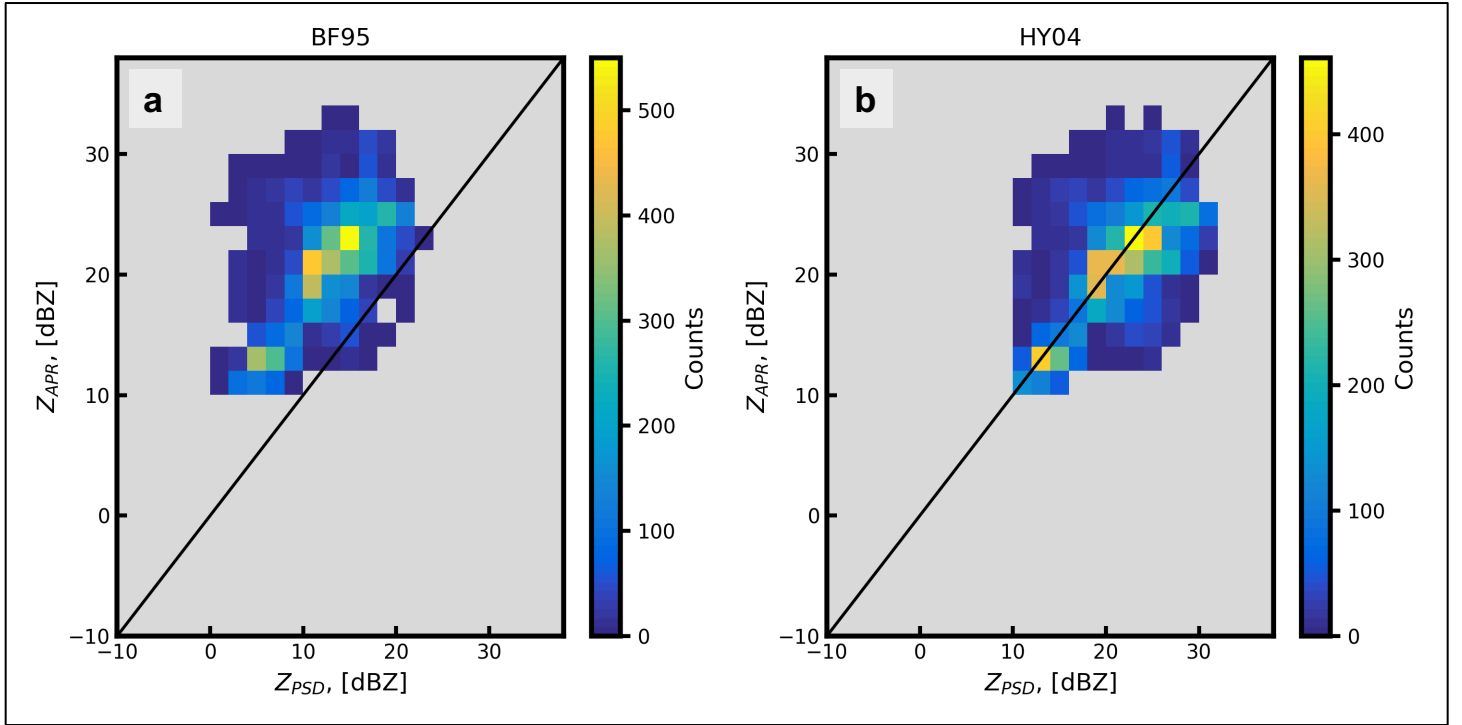


Figure 5. Comparing m - D relations and forward modeling of radar reflectivity using the Hogan et al. (2012) Rayleigh-Gans spheroid approximation using the (a) coefficients from the Brown and Francis (1995) adapted to particle maximum dimension following Hogan et al. (2012) and (b) coefficients from Heymsfield et al. (2004).

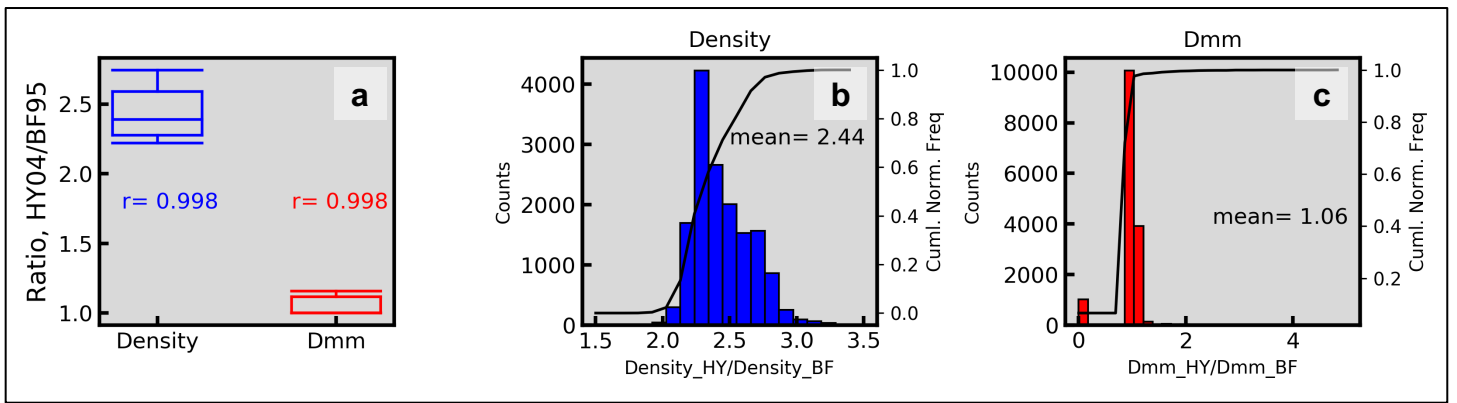


Figure 6. Comparing m - D relations and the effect on calculated PSD parameters. (a) Box plot of the ratio of HY04 to BF95 for bulk effective density (blue) and median mass dimension (red) (b) Histogram for the ratio of HY04 to BF95 for bulk effective density (c) Histogram for the ratio of HY04 to BF95 for median mass dimension

CHAPTER 3: RESULTS AND DISCUSSION

3.1 Case Study: 3 December 2015

On 3 December 2015, a short-wave trough forced stratiform pre-frontal precipitation over the Olympic Mountains producing 24-hour rain totals greater than 200 mm on the southern slopes and around 70 mm in the western valleys. Airborne radar observations (Figure 2a-c) show a bright-band at around 2.5 km above mean sea level (ASL) and echo tops near 8 km ASL. The Citation sampled a region around 4 km ASL and at -12.5 °C just over the high terrain of the Olympic Mountains. The flight started over the southeast portion of the Olympic Mountains where the low-level flow was quasi-orthogonal to the mountain range, producing the strongest orographic forcing. This is hypothesized to explain why supercooled drizzle drops were found here (Figure 7g). Most collocated triple-frequency radar observations for this case were on the portion of the DFR plane where scattering models of spherical particles, smaller aggregates and rimed aggregates co-exist, and is hereafter termed the Region of Particle Ambiguity (RPA) since particle shape information cannot be unambiguously determined using the DFR technique (Figure 7d, polygon with black shading). At 15:19:44 UTC, matched radar gates at the Citation show DFR_{Ka-W} of 10.9 dB and DFR_{Ku-Ka} of 3.1 dB (Figure 7d, blue). Example coincident images from the HVPS3, chosen using a random number generator, resemble quasi-spherical particles (Figure 7e, blue). The D_{mm} is 1.35 mm and ρ_e is 0.16 g cm^{-3} at this time. Over the next 5 minutes as the Citation flew NW, the DFR_{Ka-W} decreased to 5.9 dB while the DFR_{Ku-Ka} remained at similar values (3.2 dB, yellow Figure 7d). Particle images over this 5 minute period became less spherical and larger, with D_{mm} rising to 2.6 mm and ρ_e decreasing to 0.08 g cm^{-3} .

Modeling results from Leinonen and Szyrmer (2015) suggest that as the degree of riming of aggregates increases, increasing ρ_e , the DFR_{Ka-W} should increase due to more non-Rayleigh

scattering effects at W-band. The case presented here is consistent with this trend, showing that as the observed $\text{DFR}_{\text{Ka-W}}$ decreases and the $\text{DFR}_{\text{Ku-Ka}}$ remains the same, ρ_e decreases.

Furthermore, HVPS3 particle images support the notion of increased riming with more compact particles at 15:19:44 UTC (Figure 7e, blue) compared to 15:24:14 UTC (Figure 7e, yellow).

3.2 DFR plane and bulk statistics

To evaluate the DFR retrieval of particle shape, ρ_e and D_{mm} , all coincident DFR and microphysical in-situ observations from OLYMPEX are shown in Figure 8. Coincident observations throughout the atmospheric column correspond to temperatures from -30°C to -0.5°C (Figure 8a). The most frequent DFR bin of all 7895 observations is found within the RPA characterized by $\text{DFR}_{\text{Ku-Ka}}$ of 0 dB and $\text{DFR}_{\text{Ka-W}}$ of 2 dB (Figure 8b, black outlined bin). Furthermore, only 32% of the OLYMPEX DFR data within stratiform clouds are found on the DFR plane where only aggregate scattering models exist. Coincident ρ_e and D_{mm} calculated from the PSD (Figure 8c,d) present the average bulk properties for the same 1 dB frequency histogram bins as in Figure 8b. The most frequent bin (outlined in black) is characterized by a mean ρ_e of 0.20 g cm^3 and a mean D_{mm} of 0.85 mm. The most frequent occurrence supports a conclusion of frequent smaller and higher ρ_e particles, potentially pristine/non-aggregated particles or small rimed aggregates within the OLYMPEX stratiform clouds. Furthermore, observations well outside the RPA (polygon), with $\text{DFR}_{\text{Ku-Ka}}$ and $\text{DFR}_{\text{Ka-W}} \geq 5 \text{ dB}$ and that are following the aggregate scattering curve *hook* in Figure 8c show larger D_{mm} , lower ρ_e particles observed at higher temperatures ($T \cong -0.5^\circ\text{C}$), which provide evidence of aggregate-like particles. For example, a particle image from the HVPS3 is included on Figure 8c, showing a large ($D \cong 20 \text{ mm}$) aggregate-like particle representative of a $\text{DFR}_{\text{Ku-Ka}} \geq 10 \text{ dB}$ and a $\text{DFR}_{\text{Ka-W}}$ of $\sim 4 \text{ dB}$. To contrast this image, additional example particle images from the HVPS3

(Figure 8d) at a similar $\text{DFR}_{\text{Ka-W}}$ but $\text{DFR}_{\text{Ku-Ka}} \leq -1$ dB indicates smaller ($D \cong 2$ mm), more spherical particles.

Comparing the results from Figure 8 to past studies, the majority (62%) of OLYMPEX observations being in the RPA (Figure 8a,b) is consistent with other airborne radar observations (Kulie et al., 2014) and spaceborne radar observations (Yin et al., 2017). Furthermore, Figure 8c,d provides additional support for the results from Kneifel et al. (2015), showing that (1) ρ_e increases as $\text{DFR}_{\text{Ku-Ka}}$ decreases and $\text{DFR}_{\text{Ka-W}}$ increases, and (2) D_{mm} increases further from the origin of the DFR plane. The ability to retrieve ρ_e from the DFR plane is demonstrated in Figure 8c but these observational results do indicate some inconsistency from regions on the DFR plane in the literature (e.g., Kneifel et al., 2015; Leinonen & Szyrmer, 2015). Figure 8c supports the results from the observational study of Kneifel et al. (2015), resembling the rotation of their DFR scattering curves, but does not show the expected covariation of ρ_e with $\text{DFR}_{\text{Ka-W}}$ that is shown in the modeling results from Leinonen and Szyrmer (2015).

3.3 Figures

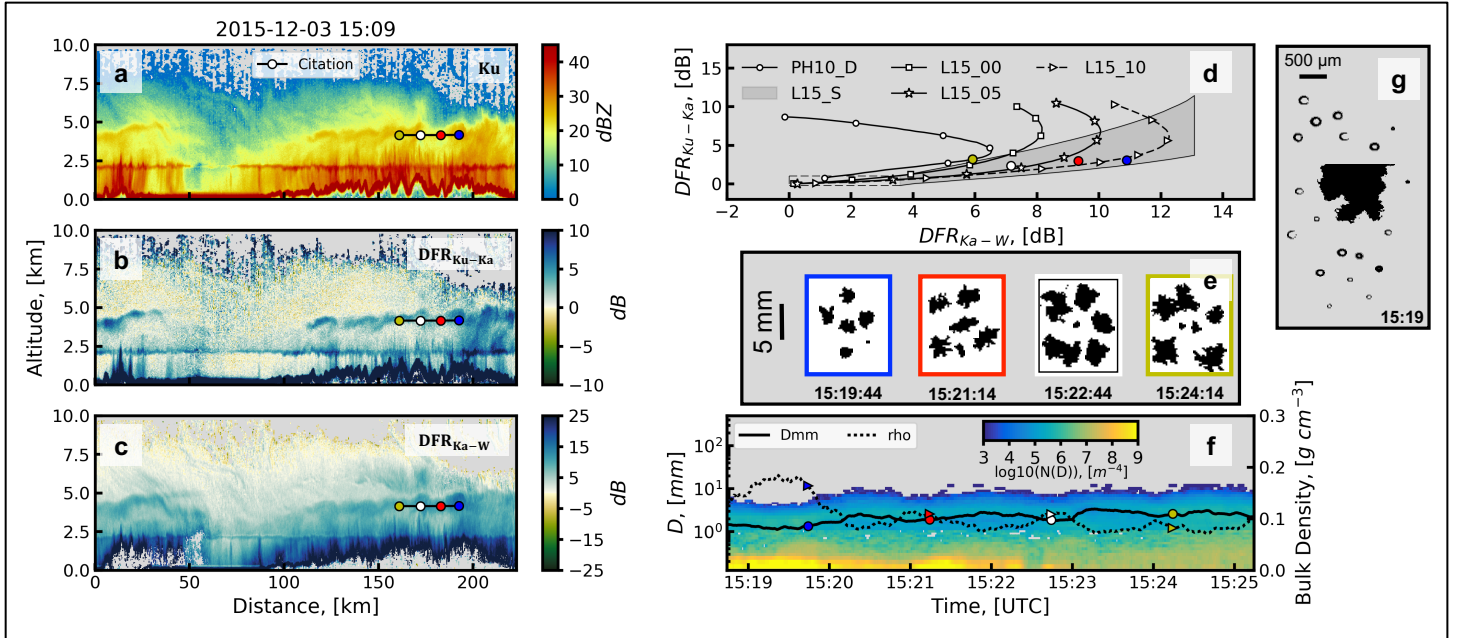


Figure 7. Vertical cross section of (a) Ku-band reflectivity, (b) DFR_{Ku-Ka} , (c) DFR_{Ka-W} measured by the APR-3 (corrected following Section 2.4), with UND Citation track overlaid with a colored marker every 90 s corresponding to colors in other subplots. Colors in order of time are blue, red, white and yellow (d) DFR plane containing scattering model curves of a dendrite aggregate (PH10_D) adapted from Petty & Huang (2010), dendrite aggregates with 0, 0.5 and 1 kg m⁻² of rime ice (L15_00, L15_05, and L15_10 respectively) adapted from Leinonen & Szyrmer (2015), and 90% of spheroid approximation for aggregates (L15_S, black shaded) adapted from Leinonen & Szyrmer (2015). The polygon is the inferred region where both complex and simple scattering models exist. Colored points are 10 s means of matched DFR values at markers in Figure 2a-c (e) Randomly selected HVPS3 particle images corresponding to the colors/times from Figure 2d (f) $N(D)$ (shading), D_{mm} (solid circles) and ρ_e (dotted triangles) along the flight track of the Citation in Fig. 2a-c (g) Sample 2DS images from 15:19, showing numerous out of focus spherical particles, inferred to be supercooled drizzle drops.

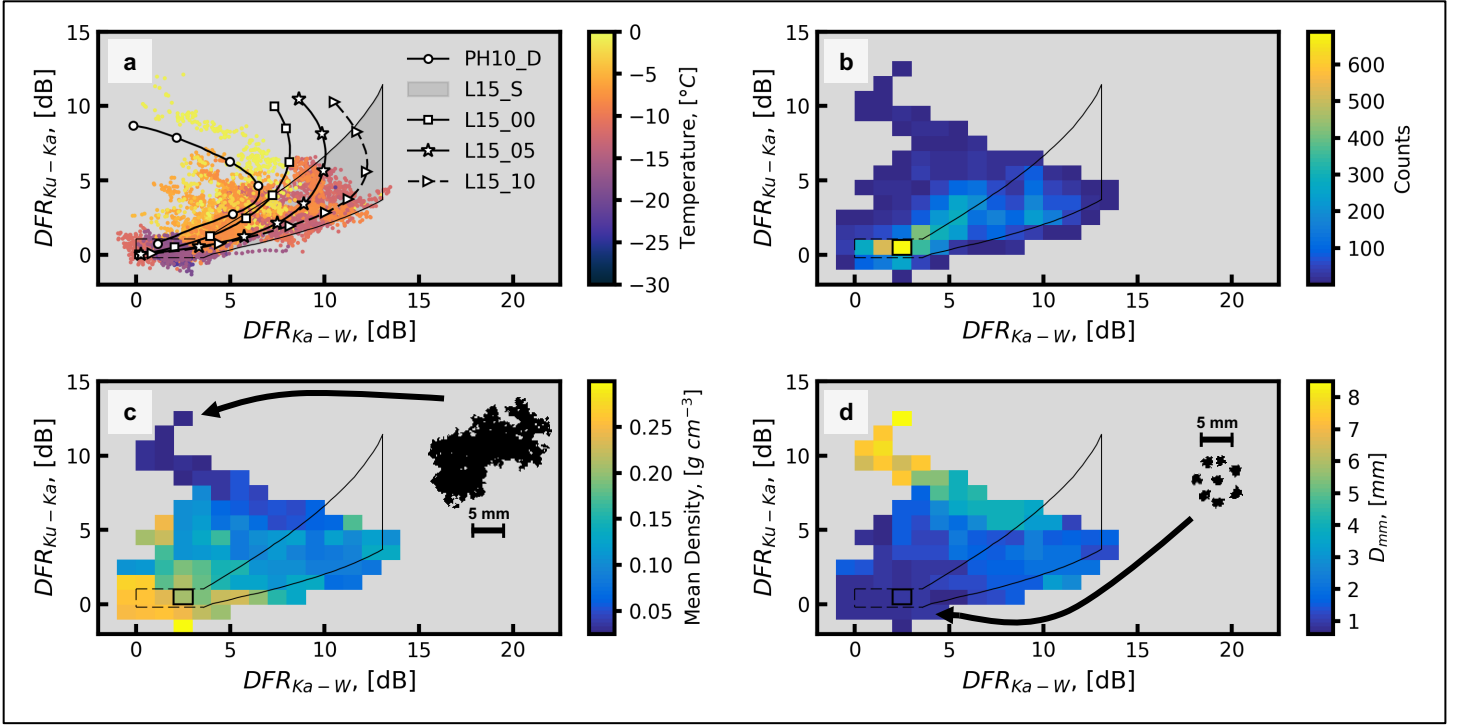


Figure 8. DFR plane using all 15 matched stratiform flight legs. **(a)** Scatterplot of all matched instances between the APR-3 and the Citation colored by observed temperature. Curves and polygon are the same as in Figure 7d. **(b)** Joint frequency of occurrence of DFR_{Ku-Ka} versus DFR_{Ka-W} , most frequent bin outlined in black. The polygon outlines the region where particle shape is ambiguous. **(c)** Using the identical 2-D histogram in Figure 3b but bins are colored by the mean ρ_e within the bin. Black silhouette is an example particle image from the HVPS3 at the indicated region on the DFR plane. **(d)** Idem Figure 8c but colored by mean D_{mm} in each bin. Black silhouettes are particle images from the HVPS3 at the indicated region on the DFR plane.

CHAPTER 4: CONCLUSIONS

Data collected in late 2015 during the Olympic Mountains Experiment (OLYMPEX, Houze et al., 2017) represent a first-of-its-kind dataset of airborne triple-frequency radar measurements coincident with airborne microphysical observations. A first-order liquid, gas and ice attenuation correction of the W-band reflectivity using in-situ observations (Section 2.4) allows for the direct evaluation of past work on triple-frequency radar snow/ice property retrievals (e.g., Kneifel et al., 2011; Kneifel et al., 2015; Leinonen & Szyrmer, 2015).

In-situ particle images obtained on 3 December 2015 coincident with triple-frequency radar observations show that particle shape information cannot be unambiguously retrieved since radar observations were found within a region outlined by scattering models of both rimed aggregates and spheroids (termed the Region of Particle Ambiguity, polygon Figure 7d). In fact, the bulk statistics of 15 flight legs reveal that few (32%) of the collected OLYMPEX in-cloud observations are found on the Dual Frequency Ratio (DFR) Ku-Ka-W plane where only aggregate scattering models exist, highlighting an important issue regarding the retrieval of particle shape from the DFR plane.

Previous modeling studies show that aggregates scatter differently than spherical/spheroidal particles but require unrimed aggregates (e.g., Kneifel et al., 2011; Leinonen & Moisseev, 2015) or large rimed aggregates (e.g., Leinonen & Szyrmer, 2015) to be present. If unrimed aggregates or large rimed aggregates are infrequent throughout the atmospheric column then the benefits of using the DFR plane to retrieve particle shape information to constrain *a priori* assumptions in the precipitation rate of ice (R) and the ice water content (IWC) retrievals might be limited. Triple-frequency observations from other studies (Kulie et al., 2014; Yin et al., 2017) also show observations are more frequently found in the Region of Particle Ambiguity.

Furthermore, the uncertainty in correcting for ice and liquid water extinction without coincident in situ measurements, the latter of which may be highly variable and not correlated with radar reflectivity in the column, may hamper the ability of retrievals using W-band to differentiate particle habit. However, studies of ice clouds in colder, less rimed conditions may yield a more comprehensive evaluation of the potential of such retrievals.

In terms of evaluating the ability of DFR retrievals of bulk particle properties, it is found that:

- a. The case study on 3 December 2015 shows in-situ bulk effective density (ρ_e) increases with increasing coincident measurements of $\text{DFR}_{\text{Ka-W}}$ (Figure 7d).
- b. Bulk effective density from all coincident points generally increases with decreasing $\text{DFR}_{\text{Ku-Ka}}$ (Figure 8c).
- c. Median mass dimension (D_{mm}) increases away from the origin of the DFR plane, with increasing $\text{DFR}_{\text{Ku-Ka}}$ and $\text{DFR}_{\text{Ka-W}}$ (Figure 8d).

These results support the retrieval of D_{mm} and ρ_e using triple-frequency radar observations. Information on these key bulk microphysical parameters are included in the $\text{DFR}_{\text{Ku-Ka}}$ and $\text{DFR}_{\text{Ka-W}}$, with more information regarding D_{mm} and ρ_e suggested in $\text{DFR}_{\text{Ku-Ka}}$. Since the Global Precipitation Measurement (GPM, Hou et al., 2014) mission collects $\text{DFR}_{\text{Ku-Ka}}$, there is potential for developing improved ice cloud property retrievals for the GPM mission as well as for future multi-frequency ground- and satellite-based multi-frequency radar measurements.

REFERENCES

- Austin, R. T., Heymsfield, A. J. & Stephens G. L. (2009). Retrieval of ice cloud microphysical parameters using the CloudSat millimeter-wave radar and temperature. *Journal of Geophysical Research*, 114, D00A23, doi: 10.1029/2008JD010049
- Barnes, S. L. (1964). A technique for maximizing details in numerical weather map analysis. *Journal of Applied Meteorology*, 3, 396 – 409
- Brown, P. R., A. & Francis, P. N. (1995). Improved measurements of the ice water content in cirrus using a total-water probe. *Journal of Atmospheric and Oceanic Technology*, 12, 410 – 414
- Cober, S. G., Isaac, G. A., Korolev, A. V. & Strapp J. W. (2001). Assessing cloud-phase conditions. *Journal of Applied Meteorology*, 40, 1967 – 1983
- Delanoë, J., Hogan, R. J., Forbes, R. M., Bodas-Salcedo, A. & Stein, T. H. M. (2011). Evaluation of ice cloud representation in ECMWF and UK Met Office models using CloudSat and CALIPSO data. *Quarterly Journal of the Royal Meteorological Society*, 137, 2064 – 2078, doi: 10.1002/qj.882
- Field, P. R., Wood, R., Brown, P. R. A., Kaye, P. H., Hirst, E., Greenaway R. & Smith J. A. (2003). Ice particle interarrival times measured with a fast FSSP. *Journal of Atmospheric and Oceanic Technology*, 20, 249 – 261
- Heymsfield, A. J., Bansemer, A., Schmitt, C., Twohy, C. & Poellot, M. R. (2004). Effective ice particle densities derived from aircraft data. *Journal of Atmospheric Sciences*, 61, 982 – 1003
- Hogan, R. J., Tian, L., Brown, P. R. A., Westbrook, C. D., Heymsfield, A. J. & Eastment, J. D. (2012). Radar scattering from ice aggregates using the horizontally aligned oblate

- spheroid approximation. *Journal of Applied Meteorology and Climatology*, 51, 655 – 671, doi: 10.1175/JAMC-D-11-074.1
- Hou, A. Y., Kakar, R. K., Neeck, S., Azarbarzin, A. A., Kummerow, C. D., Kojima, M., Oki, R., Nakamura, K. & Iguchi, T. (2014). The global precipitation measurement mission. *Bulletin of the American Meteorological Society*, 95, 701 – 722.
- Houze, R. A. Jr., McMurdie, L. A., Petersen, W. A., Schwaller, M. R., Baccus, W., Lundquist, J. D., Mass, C. F., Nijssen, B., Rutledge, S. A., Hudak, D. R., Tanelli, S., Mace, G. G., Poellot, M. R., Lettenmaier, D. P., Zagrodnik, J. P., Rowe, A. K., Dehart, J. C., Madaus, L. E. & Barnes, H. C. (2017). The Olympic Mountains Experiment (OLYMPEX). *Bulletin of the American Meteorological Society*, 98, 2167 – 2188, doi: 10.1175/BAMS-D-16-0182.1
- Jackson, R. C., McFarquhar, G. M., Stith, J., Beals, M., Shaw, R. A., Jensen, J., Fugal, J. & Korolev A. (2014). An assessment of the impact of antishattering tips and artifact removal techniques on cloud ice size distributions measured by the 2D cloud probe. *Journal of Atmospheric and Oceanic Technology*, 31, 2567 – 2590, doi: 10.1175/JTECH-D-13-00239.1
- Kneifel, S., Kulie, M. S. & Bennartz, R. (2011). A triple-frequency approach to retrieve microphysical snowfall parameters. *Journal of Geophysical Research*, 116, D11203, doi: 10.1029/2010JD015430
- Kneifel, S., von Lerber, A., Tiira, J., Moisseev, D., Kollias, P. & Leinonen, J. (2015). Observed relations between snowfall microphysics and triple-frequency radar measurements.

- Journal of Geophysical Research: Atmospheres*, 120, 6034 – 6055, doi:
10.1002/2015JD023156
- Korolev A., Strapp, J. W., Isaac, G. A. & Emery, E. (2013). Improved airborne hot-wire measurements of ice water content in clouds. *Journal of Atmospheric and Oceanic Technology*, 30, 2121 – 2131
- Kulie, M. S., Hiley, M. J., Bennartz, R., Kneifel, S. & Tanelli, S. (2014). Triple-frequency radar reflectivity signatures of snow: Observations and comparisons with theoretical ice particle scattering models. *Journal of Applied Meteorology and Climatology*, 53, 1080 – 1098, doi: 10.1175/JAMC-D-13-066.1
- Leinonen, J., Kneifel, S., Moiseev, D., Tyynelä, J., Tanelli, S. & Nousiainen, T. (2012). Evidence of non-spheroidal behavior in millimeter-wavelength radar observations of snowfall. *Journal of Geophysical Research*, 117, D18205, doi: 10.1029/2012JD017680
- Leinonen, J., & Moiseev, D. (2015). What do triple-frequency signatures reveal about aggregate snowflakes? *Journal of Geophysical Research: Atmospheres*, 120, 229 – 239, doi: 10.1002/2014JD022072
- Leinonen, J., & Szyrmer, W. (2015). Radar signatures of snowflake riming: A modeling study. *Earth and Space Science*, 2, 346-358, doi: 10.1002/2015EA000102
- Matrosov, S. Y. (2007). Modeling backscatter properties of snowfall at millimeter wavelengths. *Journal of Atmospheric Sciences*, 64, 1727 – 1736, doi: 10.1175/JAS3904.1
- Meneghini, R. & Kozu, T. (1990). *Spaceborne Weather Radar*, Boston: Artech House.
- Petty, G. W. & Huang, W. (2010). Microwave backscatter and extinction of soft ice spheres and complex snow aggregates. *Journal of Atmospheric Sciences*, 67, 769 – 787, doi: 10.1175/2009JAS3146.1

- Schwarzenboeck, A., Mioche, G., Armetta, A., Herber, A. & Gayet, J. -F. (2009). Response of the Nevzorov hot wire probe in clouds dominated by droplet conditions in the drizzle size range. *Atmospheric Measurement Techniques*, 2, 779 – 788.
- Stein, T. H. M., Parker, D. J., Hogan, R. J., Birch, C. E., Holloway, C. E., Lister, G. M. S., Marsham, J. H. & Woolnough, S. J. (2015). The representation of the West African monsoon vertical structure in the Met Office Unified Model: an evaluation with CloudSat. *Quarterly Journal of the Royal Meteorological Society*, 141, 3312 – 3324.
- Strapp, J. W., Oldenburg, J., Ide, R., Lilie, L., Bacic, S., Vukovic, Z., Oleskiw, M., Miller, D., Emery, E. & Leone, G. (2003). Wind tunnel measurements of the response of hot-wire liquid water content instruments to large droplets. *Journal of Atmospheric and Oceanic Technology*, 20, 791 – 806.
- Tanelli, S., Durden, S. L. & Im, E. (2006). Simultaneous measurements of Ku- and Ka-band sea surface cross-sections by an airborne radar. *IEEE Geosci. Remote Sens. Lett.*, 3, 359 – 363.
- Yin, M., Liu, G., Honeyager, R. & Turk, F. J. (2017). Observed differences of triple-frequency radar signatures between snowflakes in stratiform and convective clouds. *Journal of Quantitative Spectroscopy & Radiative Transfer*, 193, 13 – 20, doi: 10.1016/j.jqsrt.2017.02.017